Comparison between VLM and CFD Maneuver Loads Calculation at the Example of a Flying Wing Configuration

Arne Voss[1]

(Received: July 7, 2019. Revised: Dec 18, 2019. Accepted: Dec 27, 2019)

Abstract
This work presents the results of computational fluid dynamics (CFD) based maneuver loads calculations for a flying wing configuration. Euler solutions of the DLR Tau code are compared to vortex lattice method (VLM) results for maneuver loads in the preliminary design stage. The trim parameters of the quasi-steady maneuver load case, the structural deformation and the flow solution are determined in an iterative process. The focus is on a comprehensive loads analysis including a broad selection of load cases to cover the whole flight envelope. This is necessary to ensure a thorough preliminary design. Integration of this approach in an automated, preliminary design process and application of parametric, aeroelastic modeling allows to perform structural optimization loops to evaluate the difference between VLM and CFD on the structural design in terms of structural net mass.

1. Motivation and Introduction

The design process for new aircraft configurations is complex, costly, and involves various disciplines like aerodynamics, structure, loads analysis, aeroelasticity, flight mechanics, and weights. The task is to substantiate the selected design, based on physically meaningful simulations and analyses. Modifications are much more costly at a later stage of the design process. Thus, the preliminary design should be as good as possible to avoid "surprises" at a later stage. Therefore, load requirements are included from the certification specification already in the preliminary design. In addition, flying wings have unique characteristics that need to be considered. Next to an unconventional structural layout and a sensitive longitudinal stability, strong three-dimensional flow characteristics and transonic effects have an influence on the structural design and should be included in the preliminary design of flying wings. The aim is to include these effects as good and as early as possible. This is a trade off, because the corresponding analyses require a detailed knowledge and models, which become available only later during the design process. New methodologies in the form of a comprehensive, automated design process and a parametric aeroelastic modeling are developed.

The MULDICON: The aircraft considered in this work is an example for a swept flying wing of low aspect ratio, operating at high Mach numbers. It is a generic, multidisciplinary configuration with a half wing span of 7.69 m and a reference chord length of 6.0 m as indicated in Figures 2a and 2b. It is designed for a maximum take-off mass of 15.0 t with a payload of 2.0 t and a design Mach number of 0.8. The high leading edge sweep angle of $\pm 52°$ and the trailing edge sweep angle of $\pm 30°$ are characteristic for this configuration.

Evolution of aeroelastic models: First aeroelastic models have been developed based on the Saccon and DLR-F17 geometries and already use parametric aeroelastic modeling techniques to set-up finite element models. Those models are embedded in a multidisciplinary conceptual design process presented by Krüger et al. [9]. In a first approach, the geometry is assumed to be similar to the wing box of a classical aircraft. The resulting models were used by G. Voss

[1] Research Engineer, DLR - German Aerospace Center, Institute of Aeroelasticity, Göttingen, Germany, arne.voss@dlr.de

doi:10.3293/asdj.2019.52

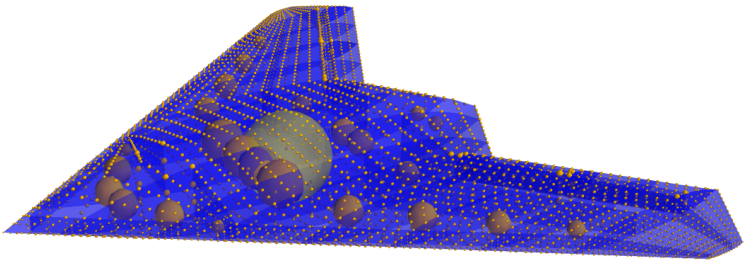

Figure 1: The MULDICON structural layout and mass discretization of the basic flight design mass (BFDM).

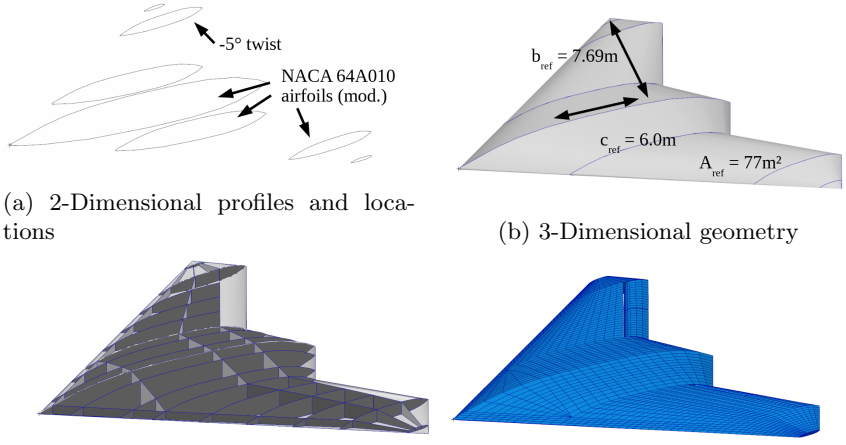

(a) 2-Dimensional profiles and locations

(b) 3-Dimensional geometry

(c) Geometrical layout with spars and ribs

(d) Geometrical layout, meshed with finite elements

Figure 2: From 2-Dimensional model information to FE model.

et al. for studies of steady aeroelastic effects [28]. The conceptual design of the DLR-F19 is refined further by Liersch et al. [14, 13], who performed multidisciplinary studies for the conceptual design of the MULDICON (Figure 1). The authors include experts of various disciplines, their tools and knowledge even in the very beginning of the design. In a successive work, Voß and Klimmek [26] developed a parametric structural model of the DLR-F19-S configuration for loads and aeroelastic analysis. Schäfer et al. [17] then assessed the phenomena of body-freedom flutter on that configuration. Using a similar, multidisciplinary approach, Liersch [15] developed a conceptual design for the MULDICON. The conceptual design comprises the planform and a structural layout with respect to the spaces required for fuel tanks, payload, landing gear, engine, etc. The aeroelastic modeling of the MULDICON (Figure 2) is performed by Bramsiepe et al. [3]. The dynamic aeroelastic stability of that configuration is evaluated by Schreiber et al. [18]. The open and closed loop gust encounter is studied by Voß [22, 24]. A general overview of aeroelastic design activities with respect to flying wings is presented by Voß et al. [27].

This work: The focus of this work is the comparison and replacement of low fidelity panel methods by higher fidelity aerodynamics within a comprehensive maneuver loads analysis and structural sizing process during preliminary design. The results of computational fluid dynamics (CFD) are compared to the vortex lattice method (VLM) and evaluated in terms of structural net mass. At the stage of preliminary design, the Euler solution appears to be a suitable choice, but may be replaced easily by a higher fidelity CFD solution at a later stage of the design process, as discussed in Section 3.2.

The aeroelastic modeling of the MULDICON is detailed in a previous work and briefly summarized in Section 2.. The theoretical background of this work is described in Section 3.. The selected maneuver load cases are presented in Section 4.. With this basis, two examples at low and high speed are studied in

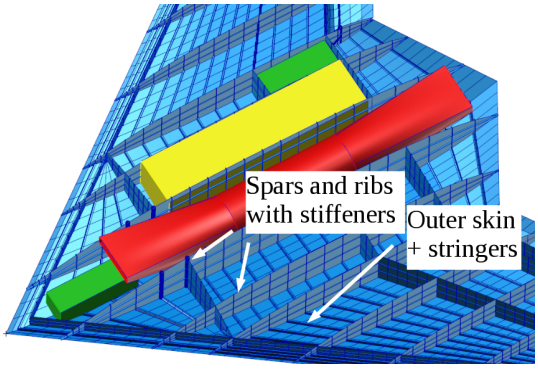

Figure 3: Inner, structural layout and FE modeling with spaces for engine (red), payload (yellow) and landing gears (green).

Sections 5. and 6.. Similarities and differences between VLM and CFD based maneuver loads are shown. For a horizontal level flight at low speed, CFD and VLM should converge and deliver similar results in terms of trim parameters and aerodynamic pressure distribution. For high speed cases, different physical effects occur and their influence is discussed. Then, all maneuver load cases are calculated using high fidelity aerodynamics within the preliminary design process. Section 7. shows the results of all 306 maneuver load cases in terms of section loads. In Section 8., the influence on the structural mass is evaluated by application of parametric modeling and an automated design process, resulting in a final aeroelastic model, optimized for minimum structural weight. Finally, in section 9., the differences between the Euler and a RANS solution are evaluated for one selected case at horizontal level flight.

Note that this work presents an extension of [23]. The manuscript has been revised and comments from the audience are answered. With respect to the results, the comparison between the Euler and RANS solution (section 9.) has been added.

2. Weight Optimized Structural and Mass Model

The aeroelastic models of the MULDICON were built and optimized for structural weight in a previous work by Bramsiepe, Voß and Klimmek [3, 26, 27]. The structural and mass models are set-up using a parametric design process. Starting with general information of the aircraft layout, a parametric geometry model is generated using the in-house software ModGen [8]. For the MULDICON, the profiles and the planform are provided. From that information, three dimensional segments are constructed, one between each of the profiles, as shown in Figures 2a and 2b. The positions of spars and ribs are defined, resulting in the model shown in Figure 2c. That geometrical layout is spatially discretized using finite elements, plotted in Figure 2d. In the case of the MULDICON, mainly shell elements are used. Beam elements are added as stiffening elements for the spars and ribs. For the upper and lower skin, stringers with hat profiles support the shell elements. Figure 3 shows the inner layout with space for the engine, the payload bay as well as the nose and main landing gear bays.

The material of the shell elements is carbon fiber reinforced plastic (CFRP). Several layers of unidirectional (UD) fibers are stacked to a laminate. The mechanical properties of the laminate can be traced back to the properties of the individual layers. The calculation principles are based on the classical laminate theory (CLT). A very useful summary of the state of the art and practical advice on the development and analysis of CFRP components is published by the Verein Deutscher Ingenieure in guideline VDI 2014, Part 3 [11], available in German and English.

The engine mass is derived from a related design task by Becker et al. [2] and Nauroz [16]. Masses for the landing gears are estimated using an in-house software. The fuel tanks are modeled geometrically using ModGen and filled to

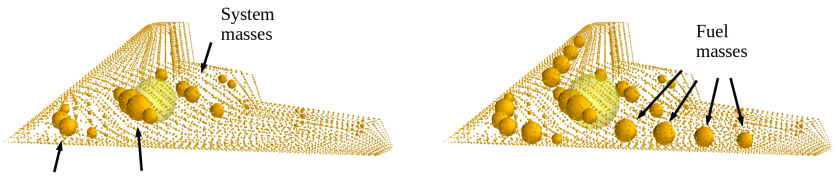

Figure 4: Two exemplary mass configurations of the MULDICON.

(a) Structure and system masses

(b) Structure, system masses and fuel masses

a required level. With this procedure, the mass, inertia and center of gravity for each section between two ribs and spars is analyzed numerically. There are two fuel tanks per side, one along the wing and a smaller one in the aircraft nose. The fuel states range from empty, through half full to full. Because the allowed travel of the center of gravity is very small, a fuel system failure would result in a loss of the aircraft and needs not to be considered for loads analyses. For additional systems, masses are estimated using conceptual design approaches. The corresponding mass discretization is shown in Figures 4a and 4b. Nine different mass configurations ranging from 5.9 t (no fuel, no payload) to 13.1 t (full fuel, full payload) are used to reflect different phases of flight during the mission. The dynamic analysis of the stiffness and mass model should result in almost only global modes for a specified frequency range. Local modes are to be avoided. Because the configuration is rather stiff, only the first 10-19 modes will be considered in this study. The selected number of modes is determined for each mass configuration individually, as the eigenfrequencies change significantly with the mass configuration.

In a next step, the structural model is subject to an optimization using MSC.Nastran SOL200. The design objective is minimum structural weight. The design variable is the skin thickness of every design field, with one design field being the area between two ribs and spars, while the topology of the structural layout, see Figure 2 and Figure 3, remains unchanged. As constraints, the failure index (FI) of the CFRP material is evaluated. For the MULDICON, the Tsai-Hill criterion by Azzi and Tsai [1] is selected. During the optimization process of the structural model, a total of 306 maneuver load cases are taken into account. These load cases are computed using the Loads Kernel software, the dimensioning load cases are identified using loads envelopes and then transferred to SOL200 as nodal loads via FORCE and MOMENT cards.

The design is an iterative procedure. After three outer loops of loads calculation followed by an optimization, convergence is achieved. The resulting model has a structural net mass of 1500 kg and a material thickness distribution as shown in Figure 17. Although the dimensioning criterion is selected conservatively, the material thickness is in most areas the minimum thickness of 2.5 mm and only some regions along the leading edge and at the wing tip are reinforced. This can be explained by the geometrical shape, which is rather thick in the center region to accommodate the engine and to provide space for payload, fuel and other aircraft systems. At the same time, the wing is very short and thus causes comparatively low bending moments. Removing some structural members could result in an even lighter design. However, most spars and ribs are required for the attachment of aircraft systems or serve as fuel bays. Ribs are also required to maintain the shape of the airfoil. Although payload and landing gear bays are planned, the outer skin is closed in the structural model. Additional cutouts for payload and landing gear doors might weaken the structure, leading to a different result. Investigations on this topic are ongoing and not subject of this article.

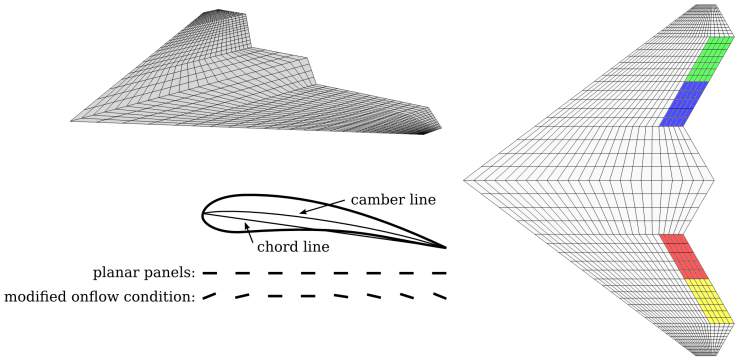

Figure 5: Aerodynamic panel mesh of the MULDICON and modeling of camber and twist.

3. Aerodynamic Models and Aero-Structural Coupling

3.1 Vortex Lattice Method

The classical aerodynamic approach with the steady Vortex Lattice Method (VLM) is chosen for this work. The formulation of the VLM follows closely the derivation given by Katz and Plotkin [7] using horse shoe vortices, where the two legs of each horse shoe vortex extend to infinity, modeling the wing wake. Compressibility effects (in the subsonic regime) are accounted for by the Prandtl-Glauert transformation with $\beta = \sqrt{1 - Ma^2}$, as suggested by Hedman [6]. The geometry is discretized using an aerodynamic panel mesh as sketched in Figure 5. The creation of such a gird for the MULDICON bears some difficulties, which are discussed briefly in the following. The first consideration concerns the number of panels in chord-wise direction. In this case, 24 panels in chord directions are selected, which is already a fairly high number for panel methods and thus discretizes the pressure distribution adequately. Also, that number allows to calculate unsteady aerodynamics in an sufficient range of reduced frequencies, which are subject in a different paper [24]. A second, important consideration concerns the aspect ratio of the panels, with a maximum aspect ratio of $AR < 3 \ldots 4$. At the wing tip of the MULDICON, this would lead to a great number of tiny panels. In addition, the panels of the last strip would need to be triangles to model the pointed shape of the wing tip. In order to avoid numerical problems, the outer wing tip is not modeled. This is a reasonable solution as the area is small and the aerodynamic contributions are considered to be negligible. For the modeling of the control surfaces, the panels have to be placed in such a way that the panel boundaries coincide with the control surfaces boundaries. In this case, they are located along the trailing edge and the inner and outer control surfaces are discretized using 5x5 and 5x7 panels, respectively. In general, the discretization of such a highly swept geometry needs to be a compromise between the long wing root and the short wing tip. Jumps in the discretization are to be avoided. The resulting mesh is shown in Figure 5 and has 1248 panels. It includes four control surfaces along the trailing edge, which are highlighted in the top view. As can be seen from Figure 5, the aerodynamic panel mesh is planar. Still, it is possible to account for camber and twist of the profile geometry by a modification of the aerodynamic onflow condition as sketched in Figure 5. An additional downwash is added to every panel, resulting in an offset of the lift polar and a modified zero-lift coefficient. Note that, except for camber and twist, no further corrections are applied and the pure vortex lattice aerodynamics are used, including the control surfaces.

3.2 Thoughts on the Selection of a CFD Solution Scheme

Classical panel methods such as the VLM are designed for the calculation of the inviscid, subsonic flow. For low speeds and moderate Reynolds numbers, the re-

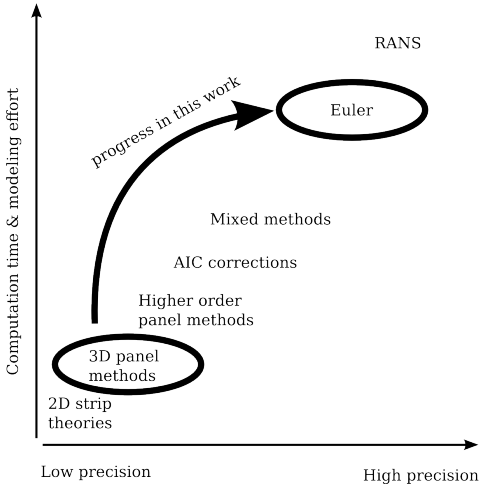

Figure 6: Comparison of aerodynamic methods in terms of precision and computation time for comprehensive loads analysis and sizing.

sults are acceptable and the agreement with higher order aerodynamic methods is usually surprisingly good with respect to loads and aeroelastic analysis. For a better description of the aerodynamic properties of an aircraft, the Navier-Stokes equations (NS), describing the viscous, compressible fluid in terms of the conservation of mass, impulse and energy, need to be solved. As of today, the solution of the full Navier-Stokes equations (DNS) is possible for small problems but not feasible for entire aircraft due to high calculation costs. Instead, the Reynolds-Averaged-Navier-Stokes equations (RANS) are a suitable choice, approximating turbulence with the help of turbulence models. The solution time for a single three dimensional flow problem ranges from several hours up to days. The next step of simplification leads to the Euler equations, neglecting viscosity and assuming an attached flow. Still, compression shocks are captured. The main drawback is the missing boundary layer due to the assumption of an inviscid flow. A thick boundary layer changes the effective shape of an airfoil, which may have an influence on a compression shock with respect to its position in chord direction. The higher the Mach and Reynolds number, the thinner the boundary layer and the more accurate the Euler solution. The solution time for a single three dimensional flow problem ranges from several minutes up to some hours. The derivation and the differences between the NS, RANS and Euler flow solutions are discussed in various textbooks on computational fluid dynamics, e.g. chapter 2.4. in reference [12].

An attempt to arrange the available flow solution schemes in terms of cost and benefit is shown in Figure 6. The diagram shows that an increase in precision always comes at the cost of higher computational times and modeling effort. Current industrial approaches are usually based on 3D panel methods such as the VLM and DLM, which are used in this work as well, in combination with an AIC matrix correction. In some cases, higher order panel methods are used. As of today, a RANS solution is the best available option but still only feasible for a few number of load cases. Considering this and the literature presented in Section 1., the following Sections present a significant progress of the aerodynamic methodologies applied within a comprehensive loads analysis and structural sizing process during preliminary design of flying wings.

In addition to the selection of the flow solution scheme, considerations should be made concerning the modeling of the problem. A good resolution of the boundary layer in a RANS calculation requires a high spatial discretization in that area, resulting not only in higher computation times but also in an increased modeling effort. In contrast, grids for Euler calculations have lower requirements and the model set-up is much easier. Comparing the convergence

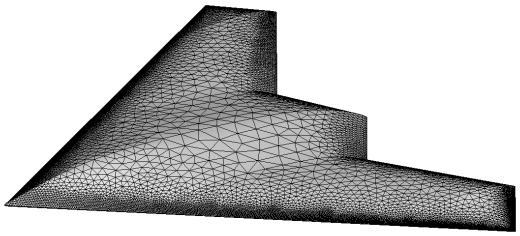

Figure 7: Unstructured surface discretization with triangles.

behavior of the iterative solution of the Euler and RANS equations, solutions of the Euler equations are usually faster and more stable than RANS equations because of the smaller size and less complexity of the problem. This results in little to no adjustments of parameters and "maintenance" during the solution process, which is an important consideration when thinking about an automated work flow for many load cases. In addition, most RANS codes have difficulties and show convergence issues for operation points in areas far away from the aircraft design point and, according to Tinoco [21], most CFD calculations are performed close to the cruise point. Krumbein [10] identifies turbulence and transition models as the weakest link in the RANS simulation chain. Reliable models are a key technology to allow for the step from Euler to RANS and still a field of research as of today. Finally, the CFD code used in this work, the DLR Tau code [19], offers both RANS and Euler solutions. This makes a switching at a later stage relatively easy.

The Euler equations seem to be an appropriate choice for this work and signify a huge improvement in terms of physical accuracy in comparison to the VLM. Since this paper focuses on aircraft loads, the comprehensive process behind the computation of the aerodynamic CFD solutions will not be elaborated on but will be accepted as a given.

For the CFD calculations, an aerodynamic mesh is required. In this work, the surface geometry generated during the model set-up using ModGen is taken, cf. Figure 2b. This ensures that the aerodynamic mesh matches exactly the remaining parts of the model in terms of size and shape. The intended CFD calculations are of inviscid nature, thus require no modeling of a boundary layer. The DLR Tau code is an unstructured CFD code and does not benefit from a structured mesh in terms of calculation time. In the case of the MULDICON, a structured mesh is difficult to realize due to the highly swept geometry, as already pointed out above concerning the VLM modeling. The advantage of surface triangles over quadrilaterals is the simple meshing procedure and the volume can be meshed with tetrahedrons only. Considering these arguments, the decision of discretization is in favor for an unstructured mesh. The resulting surface mesh is shown in Figure 7 and comprises 54,476 surface elements. The control volume is constructed using a spherical farfield with a diameter of 200 m. That volume is filled using 818,352 tetrahedrons and 153,109 nodes.

To allow for a comparison of the CFD pressure distributions with VLM, see Sections 5. and 6., the upper and lower parts of the CFD solution are projected onto the xy-plane of the VLM grid. Then, a linear interpolation is used to determine the CFD pressure coefficients at the center of each VLM panel. Finally, the upper side is subtracted from the lower side,

$$\mathbf{\Delta c}_p^{\text{CFD, interp}} = \mathbf{c}_{p,\text{lower}}^{\text{CFD, interp}} - \mathbf{c}_{p,\text{upper}}^{\text{CFD, interp}} \tag{1}$$

allowing for a comparison of the pressure distributions $\mathbf{\Delta c}_p^{\text{CFD,interp}}$ and $\mathbf{\Delta c}_p^{\text{VLM}}$.

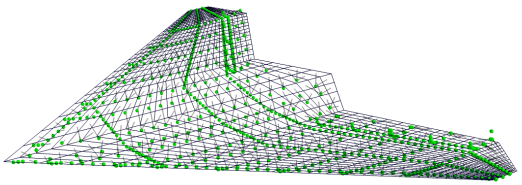

Figure 8: Aero-structural coupling of the MULDICON using a rigid body spline.

3.3 Aero-Structural Coupling

Because the VLM calculates the pressure difference $\mathbf{\Delta c_p}$ between upper and lower surface as indicated by the planar aerodynamic mesh in Figure 5, the engineer is forced to select one side only for coupling. In this case, all spars and ribs on the lower side are selected. For the VLM based solutions, the aero-structural coupling uses the rigid body spline in combination with a nearest neighbor search visualized in Figure 8. The small black lines visualize the mapping of the aerodynamic grids onto the structural grids. The theoretical background and the advantages and disadvantages of different splining strategies are discussed in [25].

Using a three dimensional CFD solution, the above restrictions could be removed and the aerodynamic forces could be distributed more evenly on both the upper and lower surface. In addition, local peaks of the nodal forces are more unlikely to occur because there are more CFD nodes than structural nodes. However, to allow for a good comparison, the CFD forces are first transferred to the VLM grid using rigid body splining techniques. Note that because CFD forces are considered in x-, y- and z-direction, and not only pressures, forces and moments are preserved and drag could be captured as well. Difficulties that might occur in relation to the mapping of pressures, e.g. at the stagnation points at the leading and trailing edges, are avoided. The CFD forces are then processed in the same way and use the same matrices as if they were from VLM. The mesh deformation of the CFD surface is performed using a volume spline to achieve smooth surface deformation.

4. Applied Load Cases

At the end of the detail design stage, the aircraft usually needs to be certified by an aviation authority, e.g. the European Aviation Safety Agency (EASA). Apart from other requirements, it has to be shown that the aircraft withstands the loads that are specified in the Certification Specifications, e.g. CS-23 [4] for small aircraft or CS-25 [5] for large aircraft, depending on the specifications that have to be applied. Therefore, it is very useful to include load requirements from the certification specification already in the preliminary design. In this work, emphasis is put on a comprehensive loads process including a large number of load cases (¿100) to cover the flight envelope to ensure a thorough preliminary design. Such a fairly high number of load cases is necessary to cover a sufficient number of flight conditions as well as to take into account that different parts of the aircraft may be sized by different design load cases. The maneuver load cases consist of two groups. Vertical maneuvers following CS 25.337 include pull up with $N_z = 2.5$, horizontal level flight with $N_z = 1.0$ and push down with $N_z = -1.0$. The load factor for push down at VD/MD is reduced to $N_z = 0.0$. They are calculated for all mass configurations, altitudes and flight speeds, resulting in 270 maneuver load cases. The vertical maneuvers are completed by a number of so-called design maneuvers that are performed at sea level, with VD and for the basic flight design mass (BFDM, 10.8 t, full payload, half fuel) only. These design maneuvers include high pull up and push down load factors, roll rates p and roll accelerations $\dot{p}$ and various combinations of them. For the following Sections, a three-step approach is chosen. First, a low speed horizontal level flight at $Ma = 0.4$ is considered, where CFD and VLM are expected to

	Number	Description
Mass configurations	9	All
Altitudes	5	FL000, FL055/FL075, FL200, FL300 and FL450
Speeds	2	VC/MC, VD/MD
Vertical maneuvers	3	Pull up, horizontal level flight, push down, for all masses, altitudes, speeds
Sub-total	270	
Design maneuvers	76	At FL000, VD and M12 only
Total	306	

Table 1: Overview of maneuver load cases.

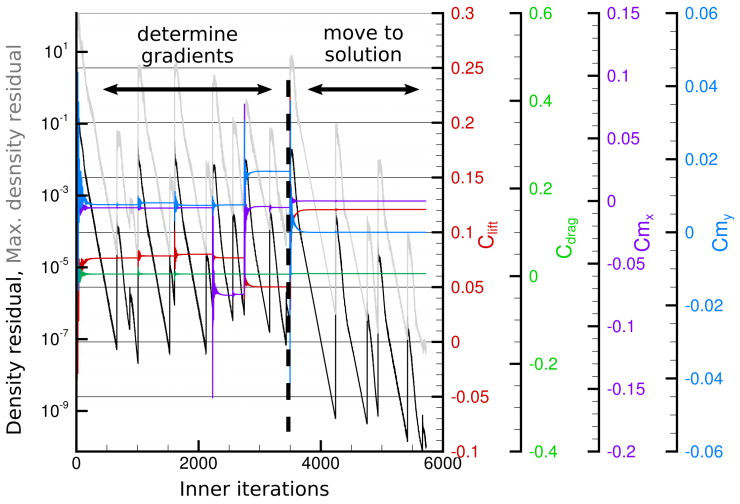

Figure 9: CFD convergence history for trim of low speed level flight.

yield similar results in terms of trim condition and pressure distribution. Second, a high speed case at $Ma = 0.9$ is investigated, where different physical effects occur and their influence is discussed. Finally, all maneuver load cases are calculated.

5. Step One: Low Speed Horizontal Level Flight

The aircraft is trimmed in a horizontal level flight at a mach number of $Ma = 0.4$ at sea level, which corresponds to a true air speed of $V_{\text{tas}} = 136.12\,m/s$ and a dynamic pressure of $q_\infty = 11348.4\,Pa$. The mass configuration is the basic flight design mass, the load factor is $N_z = 1.0$ and the required lift coefficient in z direction is $C_z = 0.1197$. The required pitching moment coefficient with respect to the moment reference point, located at $[6.0, 0.0, 0.0]$, is $C_{my} = 0.004258$ and the rolling moment coefficient is to be $C_{mx} = 0.0$. The trim variables are the angle of attack α and the pilot commands ξ and η for roll and pitch. Note that the angle of attack α is an indirect trim variable and the result of the aircraft velocities u and w. The velocities are calculated by the trim algorithm in such a way that sufficient lift is created and that the true air speed V_{tas} is matched.

During the trim calculation, the CFD code shows a convergence behavior as plotted in Figure 9. The trim results are given in Table 2. The angle of attack

Trim Solution	VLM	CFD
α	2.45°	2.49°
ξ	0.0°	−0.16°
η	−2.49°	−1.24°

Table 2: Trim solution for low speed level flight.

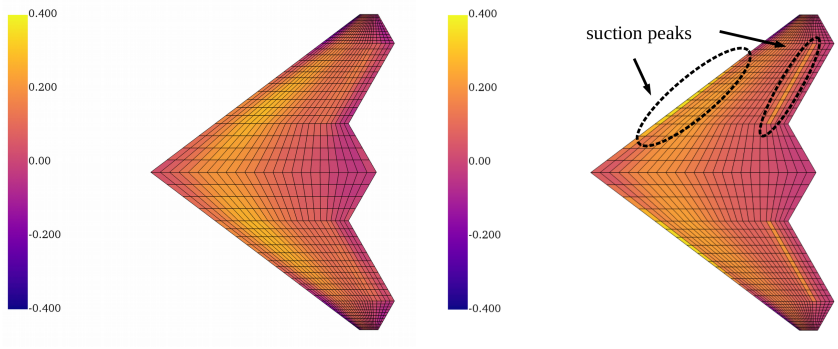

Figure 10: Pressure coefficient distributions from CFD $\mathbf{\Delta c}_p^{\text{CFD,interp}}$ (left) compared to VLM $\mathbf{\Delta c}_p^{\text{VLM}}$ (right), low speed (Ma=0.4).

α is very similar for both the CFD and the VLM solution. The aerodynamic mesh of the VLM solution, the structural and the mass model are all three perfectly symmetrical in a numerical sense. This, however, is not the case for the unstructured CFD mesh where, as described in section 3.2, the surface is discretized with triangles. This leads to a slightly asymmetric mesh and a slightly asymmetric CFD solution, requiring a small rolling command ξ for compensation. The pitching command η has a negative sign in both cases, indicating a downward deflection of the control surfaces to compensate a nose up pitching moment (the pilot pushes the stick). The pitching command η is slightly smaller for the CFD solution. Assuming similar control surface efficiency, it can be concluded that the pressure distribution of the CFD solution leads to a slightly lower pitching moment M_y than the VLM solution. Because the lift is the same in both cases (same maneuver case), this indicates that the center of pressure CP (of the untrimmed aircraft) is closer to the center of gravity CG. Note that the VLM is corrected for both camber and twist.

With the trimmed solutions, the pressure distribution on the lifting surface may be inspected for any differences. As expected from the trim results, the pressure distributions plotted in Figure 10 look similar in both magnitude and spatial distribution. Compared to CFD, the VLM solutions shows a slightly more pronounced suction peak along the leading edge and along the leading edges of the control surfaces. This can be explained by the aerodynamic approach based on potential theory. In general, good convergence is demonstrated for the numerical CFD solutions. For a horizontal level flight at low speed, CFD and VLM converge and yield similar results in terms of trim condition with small difference in pressure distribution. This is as expected and serves as a baseline for the following investigations.

Note that the calculation of one trimmed maneuver load case takes $\approx 1-2$s with VLM and $\approx$ 10h on a 24 core CPU with CFD, if the solution converges well, which depends strongly on the maneuver and the operation point.

6. Step Two: High Speed Horizontal Level Flight

For the second example, the aircraft speed is successively increased up to $Ma = 0.9$. All other parameters of the operation point remain unchanged. A summary of the trim solutions is given in Table 3. As the dynamic pressure increases with the mach number, the required angle of attack α for horizontal level flight reduces compared to the low speed case. At a mach number of $Ma = 0.8$, the CFD solution is still comparable to the VLM solution. The angle of attack α and pitching command η are slightly lower than the VLM solution. For mach numbers $Ma = 0.85$ and $Ma = 0.9$, the differences increase. While the pitching command η has been lower for the CFD solution, its magnitude increases significantly up to $\eta = -7.27°$ for the CFD solution compared to $\eta = -2.03°$ for the VLM solution.

The reason for the behavior of the trim solution is found in the surface

Trim Solution/Ma		0.4	...	0.8	0.85	0.9
VLM	α	2.45°	...	0.68°	0.60°	0.54°
	ξ	0.0°	...	0.0°	0.0°	0.0°
	η	−2.49°	...	−2.16°	−2.03°	−2.03°
CFD	α	2.49°	...	0.61°	0.54°	0.37°
	ξ	−0.16°	...	−0.05°	−0.07°	−0.13°
	η	−1.24°	...	−1.43°	−2.77°	−7.27°

Table 3: Trim solutions for low and high speed level flight.

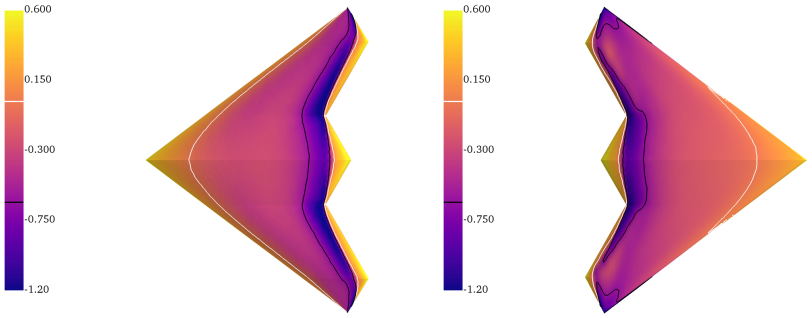

Figure 11: CFD pressure coefficient distribution $\mathbf{c}_p^{\text{CFD}}$ on upper (left) and lower (right) side, high speed.

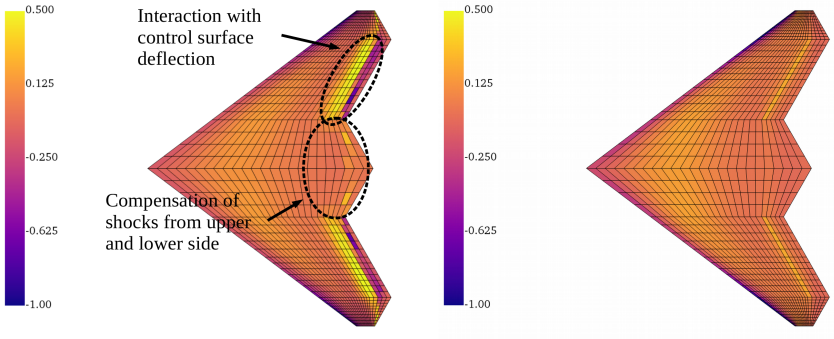

Figure 12: CFD pressure coefficient distribution $\mathbf{c}_p^{\text{CFD}}$ on upper (left) and lower (right) side, high speed.

pressure distribution of the $Ma = 0.9$ flight condition shown in Figure 11. The black line indicates the critical pressure coefficient $c_{p,\text{crit}} = -0.61$ and the white line indicates $c_p = 0.0$. Two shock systems can be identified. The first compression shock system is visible in the fuselage region. Because of the low angle of attack and the symmetrical airfoil, the shock is both visible on the upper and lower surface and approximately at the same chord position. Looking at the difference in pressure between upper and lower side $\mathbf{\Delta c}_p^{CFD,interp}$ given in Figure 12, the two shocks compensate each other. The result looks very similar to the VLM solution. However, this is more or less by coincidence and only holds for this flight condition. Higher altitudes or higher load factors might lead to higher angles of attack, resulting in different flow solutions and compression shocks at different chord positions. This could change the pitching moment significantly. A second compression shock system is visible at the wing trailing edge, where unfortunately the control surfaces are located. As the control surfaces are deflected downwards, this weakens the shock on the lower side and strengthens the shock on the upper side. This interaction has an impact on the difference in pressure $\mathbf{\Delta c}_p^{CFD,interp}$, see marked areas in Figure 12. In addition, there is a strong interaction of the location of the compression shock and the control surface deflection. This leads to strong non-linearities during the process of the trim solution. A comprehensive discussion of transonic flow patterns on flapped airfoils and different types of shocks is given in literature, see for instance chapter 3 in Tijdeman [20]. In the numerical analysis, these non-linearities are reflected in an increase of the number of function evaluations and an increase of inner aero-structural coupling iterations from 21 for the low speed case to 33.

7. Step Three: All Maneuver Load Cases

Although care has been taken, some maneuver load cases are expected to fail. Generally, three modes of failure are considered:

- Divergence of the CFD solution, indicating a very unsteady flow.
- Missing convergence of the structural deformation, indicating an unsteady, oscillating flow solution.
- Missing convergence of the trim solution because the requested maneuver is without the physically possible bounds or the solution lies without the bounds of e.g. the allowed control commands.

The pragmatic decision is that a flight under such conditions is unrealistic or the aircraft will never reach that condition. Therefore, the maneuver load case is omitted. For the real aircraft, this needs to be checked in an additional, more detailed analysis, which is unfeasible during a preliminary design process and is not the scope for this work. A first finding is that load cases exist which could not be calculated using CFD while VLM always gives a solution. This might sound rather obvious, but it is a crucial finding. It is a very good argument in favor of comprehensive maneuver loads analyses and only the engineer who includes many maneuver load cases at different altitudes, speeds, etc. will encounter and realize these boundaries. To allow for a reasonable comparison of CFD to VLM results, of course only those maneuvers that were successful in CFD should be compared. Because of the large number of maneuver load cases, an individual inspection of every case with trim conditions, pressure plots, etc., is no longer feasible. Loads envelopes are an appropriate means and will be used in the following. A direct comparison of the maneuver load envelopes from CFD and VLM is shown in Figure 13 for the right wing root. One can clearly see a shift and stretching of the loads envelopes while the shape is nearly unchanged. The minimum shear force is decreased by 2.4% while the maximum value is increased by 9.4%. The minimum bending moment is increased by 7.1% while

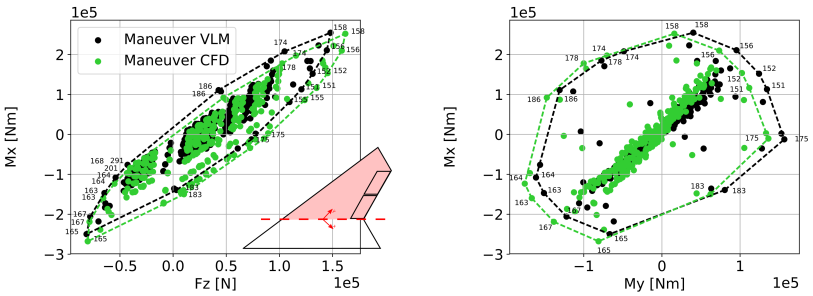

Figure 13: Loads envelope of shear force F_z, bending moment M_x and torsion moment M_y at the right wing root.

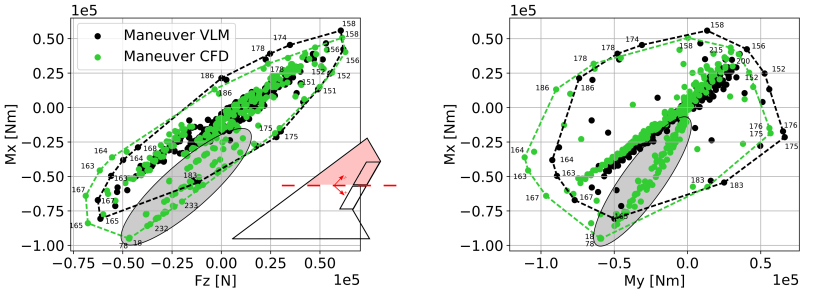

Figure 14: Loads envelope of shear force F_z, bending moment M_x and torsion moment M_y at the right outer wing.

the maximum value is decreased by 1.0%. The minimum torsional moment is increased by 8.4% and the maximum value is decreased by 13.0%. Looking at the labels that identify the dimensioning load case, one can see the same cases for VLM and CFD.

At the right outer wing, the differences are more pronounced as shown in Figure 14. While some parts of the envelopes look very similar with a moderate offset, there are some regions, as marked in the plot with grey color, which are completely different. These load cases extend the envelope significantly, especially in terms of bending moment , but the total value is still very low because of the short lever arms of the forces acting on the outer wing.

As expected from the previous studies of the high speed horizontal level flight in Section 6., the control surfaces experience a different loading using CFD. The CFD maneuver load envelopes of the inner and outer aileron, shown in Figure 15, are different from the VLM envelopes in both size and shape. While there is a similarity between the inner and outer control surface for the VLM based envelopes, the CFD envelopes show no such similarity. At the inner control surface, a high hinge moment corresponds to a high negative shear force . This is not the case for the outer control surface. Although the deflections of inner and outer control surface are of the same magnitude, the resulting shear forces are generally higher at the outer control surface. Looking at the example of maneuver load case number 175, marked with arrows in the plots, one can see that it produces the highest shear force at the outer control surface while the shear force is close to zero at the inner control surface. This might be the reason for the differences observed at the right outer wing in Figure 14.

Note that all the differences in section loads shown in Figures 13, 14 and 15 are due to the spatial distribution of the aerodynamic forces only. This is because the maneuver cases, and thus the overall forces and moments of the aircraft, are the same. Also it should be mentioned that solely the aerodynamic method is exchanged while the structural, mass and coupling models and even the loads analysis software are identical.

8. Influence in Terms of Structural Weight and Loading

In Figures 17 and 18, the resulting material thickness distribution is shown. The material thickness distribution of the CFD-based maneuver loads loop shows

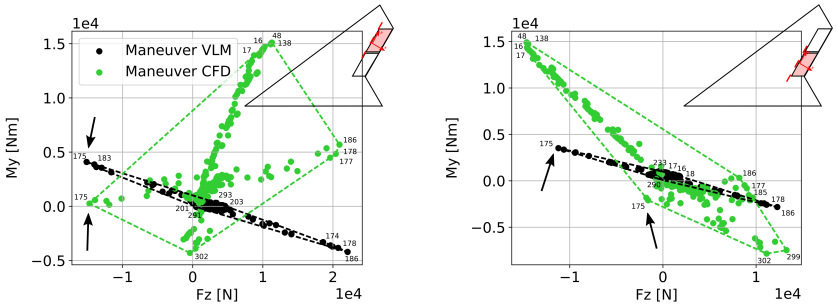

Figure 15: Envelope of control surface attachment loads.

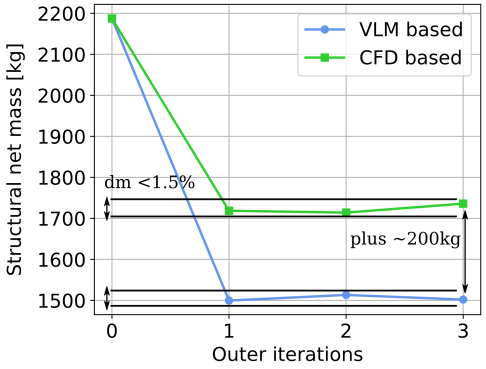

Figure 16: Convergence history of structural net mass.

similarities to the VLM-based maneuver loads loop, for example along at the front spar. Significant differences are visible along the rear spar, where the CFD-based maneuver loads cause a significant increase in material thickness. Also, the rear parts of lower skin show a material thickness of approximately 6 to 7 mm while the minimum material thickness of 2.5 mm was sufficient for the VLM-based maneuver loads loop. The changes in the rear region are likely to be caused by the transonic aerodynamics and the compression shocks observed in Section 6.. With 1735.9 kg, the resulting structural net mass is approximately 200 kg heavier than the reference. The convergence behavior is again very good as can be seen from the development of the structural net mass shown in Figure 16. In this context, the aero-structural coupling needs to be considered. As explained in Section 3., the same coupling strategy (lower side spars and ribs) is deliberately used for both VLM and CFD based maneuver loads to allow for a meaningful comparison. With a three dimensional CFD solution available, that restriction could be removed and the aerodynamic forces could be distributed more evenly on both the upper and lower surface. Presumably, this will have an impact on the prominent material thickness increases on the lower side observed in Figure 18. However, that is not the scope of this work. Note that the difference in structural mass has an influence on the location of the center of gravity CG, which has an influence on the trim condition and on loads. For mass configuration M12 (basic flight design mass) for example, the difference in x-direction is less than 1% compared to the VLM based optimization. If the shift of CG due to higher structural weight becomes too large, it could be considered to adjust the position of the payload and/or fuel masses to move the CG back to the original design location.

9. Comparison of Euler and RANS Solutions

In this work, the Euler equations have been selected for the CFD solution scheme, as discussed in Section 3.2. The main shortcoming of the Euler equations is probably the missing boundary layer. In order to judge the quality and reliability of the data, the RANS equations have been used to calculate the

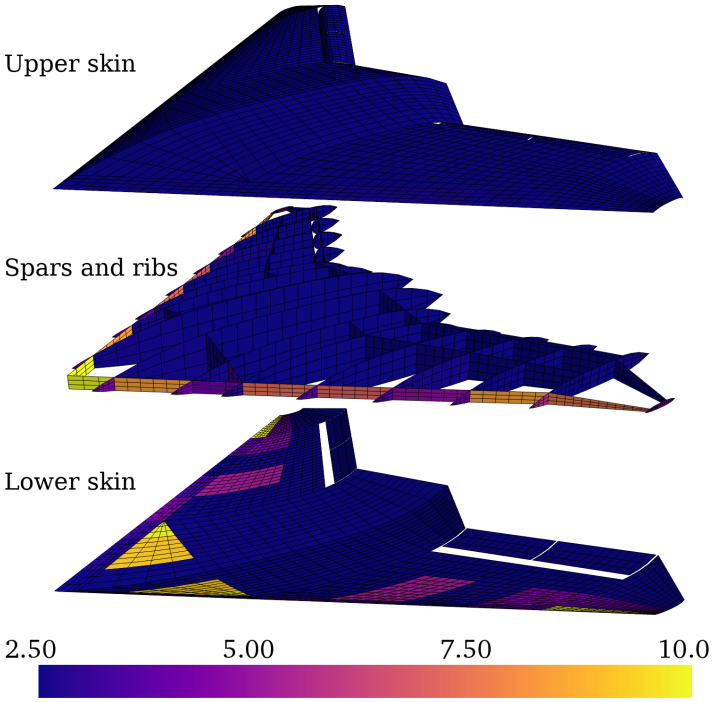

Figure 17: VLM-based maneuver loads loop: material thickness distribution of skin, spars and ribs in [mm].

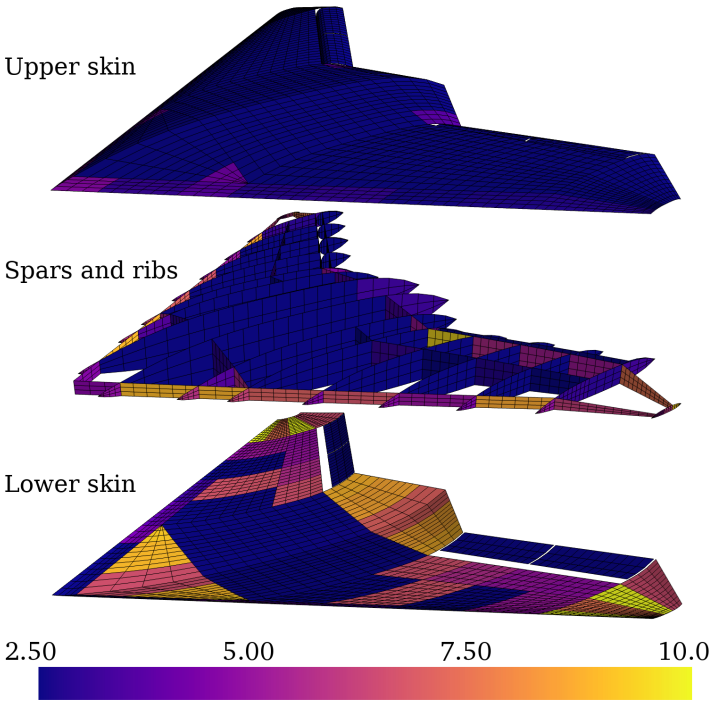

Figure 18: CFD-based maneuver loads loop: material thickness distribution of skin, spars and ribs in [mm].

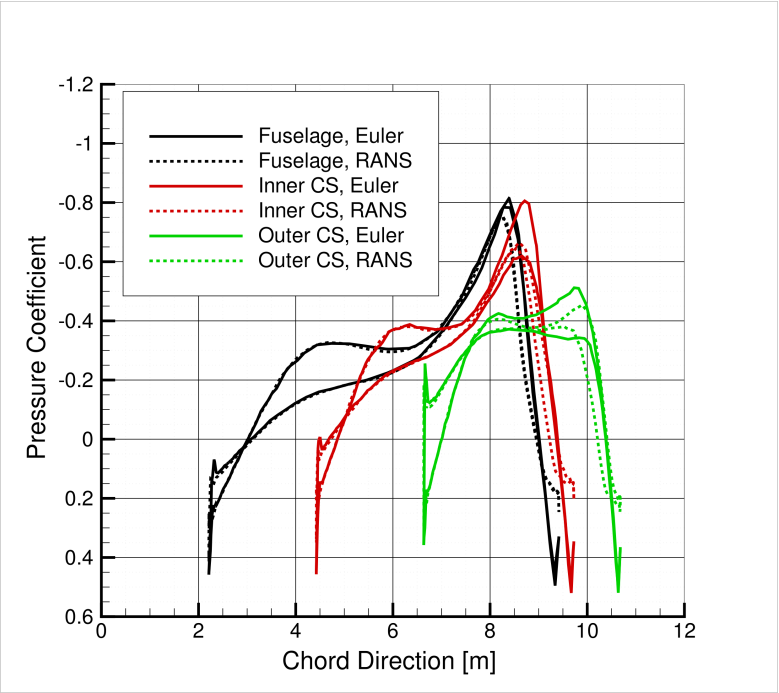

Figure 19: Comparison of Euler and RANS based pressure coefficients of trimmed horizontal level flight at $Ma = 0.8$ in the fuselage region and at the inner and outer control surfaces.

trimmed solution of one selected horizontal level flight condition at $Ma = 0.8$. In Figure 19, the pressure coefficients are shown for surface cuts at the fuselage and in the region of the inner and outer control surface. One can see there is nearly no difference between the Euler and the RANS solution in front of the compression shock, which occurs at $\approx 8.5m$, $\approx 9.0m$ and $\approx 10.0m$ in chord direction respectively. It can be seen that the compression shocks are slightly less pronounced for the RANS solutions. This is as expected, because the boundary layer becomes thicker towards the rear of the airfoil, changing its effective shape and leading to a weaker acceleration of the flow and thus to a weaker compression shock. For this particular operation point, the differences between Euler and RANS are small in terms of position and amplitude of the compression shocks, so that e.g. the influence on the overall pitching moment is small as well. Still, these difference have to be kept in mind when judging and interpreting the results.

10. Conclusion and Outlook

In this work, CFD maneuver loads for a flying wing configuration are studied in a three-step approach, first at the example of a low speed horizontal level flight, then for higher speeds and finally for all maneuver cases. Good convergence could be demonstrated for the numerical CFD solutions. For a horizontal level flight at low speed, CFD and VLM converge and deliver similar results in terms of trim conditions with small difference in pressure distribution. For higher speeds, strong transonic effects are visible. They change the pitching moment significantly, leading to different trim conditions. In addition, a compression shock just in front of / on the control surfaces substantially reduces the control efficiency.

Considering all maneuver load cases requires a failure tolerant process, because not all trim cases can be expected to converge using CFD. Especially unmindfully defined flight points might turn out to be nonphysical. Comparison of the CFD to the VLM based maneuver loads shows load envelopes at the wing root that are similar in size and shape but have an offset. At the outer wing and at the control surfaces, the envelopes take different shapes and new dimensioning load cases are identified. Those changes are reflected in the

structural optimization as well. The new structural mass is approximately 200 kg heavier than the reference.

Application of the Euler equations allows to calculated a large number of maneuver load cases and to cover the flight envelope while higher fidelity RANS equations require much higher computational times. As of today, this is still a trade-off and both objectives can not be reached simultaneously. Therefore, both solution schemes are compared at one selected horizontal level flight condition. The differences are as expected and rather small at that particular operation point.

With the CFD maneuver loads process ready for flying wings, future projects could apply the process to classical wing-fuselage-empennage configurations. Especially the fuselage would benefit from an aerodynamic method that captures its large, volumetric body adequately. Different trim conditions are expected, which have an influence on loads.

References

[1] V. D. Azzi and S. W. Tsai. Anisotropic strength of composites. *Experimental Mechanics*, 5(9):283–288, September 1965. https://link.springer.com/article/10.1007/BF02326292.

[2] R.-G. Becker, S. Reitenbach, C. Klein, T. Otten, M. Nauroz, and M. Siggel. An Integrated Method for Propulsion System Conceptual Design. In *ASME Gas Turbine Technical Congress and Exposition*, Montréal, Canada, June 2015. ASME. http://proceedings.asmedigitalcollection.asme.org/proceeding.aspx?doi=10.1115/GT2015-43251.

[3] Kjell Bramsiepe, Arne Voß, and Thomas Klimmek. Design and Sizing of an Aeroelastic Composite Model for a UCAV Configuration with Maneuver, Gust and Landing Loads. München, September 2017. Deutsche Gesellschaft für Luft- und Raumfahrt - Lilienthal-Oberth e.V. https://elib.dlr.de/114919/.

[4] European Aviation Safety Agency, editor. *Certification Specifications for Normal, Utility, Aerobatic, and Commuter Category Aeroplanes CS-23*. Amendment 3 edition, July 2012.

[5] European Aviation Safety Agency, editor. *Certification Specifications for Large Aeroplanes CS-25*. Amendment 16 edition, December 2015.

[6] Sven G Hedman. Vortex Lattice Method for Calculation of Quasi Steady State Loadings on Thin Elastic Wings in Subsonic Flow. (FFA Report 105), 1966.

[7] Joseph Katz and Allen Plotkin. *Low-speed aerodynamics: from wing theory to panel methods*. McGraw-Hill series in aeronautical and aerospace engineering. McGraw-Hill, New York, 1991.

[8] Thomas Klimmek. Parameterization of topology and geometry for the multidisciplinary optimization of wing structures. In *CEAS 2009 - European Air and Space Conference*, Manchester, United Kingdom, October 2009. Council of European Aerospace Societies.

[9] Wolf R. Krüger, Sunpeth Cumnuantip, and Carsten M. Liersch. Multidisciplinary Conceptual Design of a UCAV Configuration. In *Proceedings AVT-MP-173*, Sofia, Bulgaria, May 2011. North Atlantic Treaty Organization.

[10] Andreas Krumbein. Transition Modeling Activities at AS-CASE (DLR), 2017. https://elib.dlr.de/113935/.

[11] VDI-Fachbereich Kunststofftechnik. Entwicklung von Bauteilen aus Faser-Kunststoff-Verbund - Berechnungen. Richtlinie VDI 2014 Blatt 3, Verein Deutscher Ingenieure, September 2006.

[12] Stefan Lecheler. *Numerische Stroemungsberechnung: schneller Einstieg durch anschauliche Beispiele*. Studium. Vieweg + Teubner, Wiesbaden, 2. aktualisierte und erw. auflage edition, 2011.

[13] C. M. Liersch, K. C. Huber, A. Schütte, D. Zimper, and M. Siggel. Multidisciplinary design and aerodynamic assessment of an agile and highly swept aircraft configuration. *CEAS Aeronautical Journal*, 7(4):677–694, December 2016. http://link.springer.com/10.1007/s13272-016-0213-4.

[14] Carsten M. Liersch and Kerstin C. Huber. Conceptual Design and Aerodynamic Analyses of a Generic UCAV Configuration. In *32nd AIAA Applied Aerodynamics Conference*, Atlanta, GA, June 2014. American Institute of Aeronautics and Astronautics. http://arc.aiaa.org/doi/abs/10.2514/6.2014-2001.

[15] Carsten M. Liersch, Andreas Schütte, Martin Siggel, and Jochen Dornwald. Design Studies and Multi-Disciplinary Assessment of Agile and Highly Swept Flying Wing Configurations. In *Deutscher Luft- und Raumfahrtkongress 2018*, Friedrichshafen, Deutschland, 2018. Deutsche Gesellschaft für Luft- und Raumfahrt - Lilienthal-Oberth e.V. https://elib.dlr.de/126539/.

[16] Mobin Nauroz. Antriebskonzept einer agilen hoch gepfeilten Flugzeugkonfiguration. In *Deutscher Luft- und Raumfahrtkongress*, Rostock, September 2015. Deutsche Gesellschaft für Luft- und Raumfahrt - Lilienthal-Oberth e.V. http://elib.dlr.de/98597/.

[17] Dominik Schäfer, Cyrille Vidy, Christoph Mack, and Jürgen Arnold. Assessment of Body-Freedom Flutter for an Unmanned Aerial Vehicle. In *Deutscher Luft- und Raumfahrtkongress*, Braunschweig, September 2016. Deutsche Gesellschaft für Luft- und Raumfahrt - Lilienthal-Oberth e.V.

[18] Philip Schreiber, Cyrille Vidy, Arne Voß, Jürgen Arnold, and Christoph Mack. Dynamic Aeroelastic Stability Analyses of Parameterized Flying Wing Configurations. Friedrichshafen, September 2018. Deutsche Gesellschaft für Luft- und Raumfahrt - Lilienthal-Oberth e.V. https://elib.dlr.de/124855/.

[19] Dieter Schwamborn, Thomas Gerhold, and Ralf Heinrich. The DLR Tau-Code: Recent Applications in Research and Industry. In *European Conference on Computational Fluid Dynamics*, 2006.

[20] H Tijdeman. *Investigations of the Transonic Flow Around Oscillation Airfoils*. Dissertation, TU Delft, 1977.

[21] E. N. Tinoco, D. R. Bogue, T.-J. Kao, N. J. Yu, P. Li, and D. N. Ball. Progress toward CFD for full flight envelope. *The Aeronautical Journal*, 109(1100):451–460, October 2005. https://www.cambridge.org/core/journals/aeronautical-journal/article/progress-toward-cfd-for-full-flight-envelope/8D0D3EA36A307E597E26FA2CBA73758A#.

[22] Arne Voß. Gust Loads Calculation for a Flying Wing Configuration. Atlanta, Georgia, June 2018. American Institute of Aeronautics and Astronautics. https://arc.aiaa.org/doi/abs/10.2514/6.2018-3326.

[23] Arne Voß. Comparing VLM and CFD Maneuver Loads Calculations for a Flying Wing Configuration. In *18th International Forum on Aeroelasticity and Structural Dynamics*, Savannah, Georgia, June 2019. https://elib.dlr.de/127750.

[24] Arne Voß. Open and closed loop gust loads analyses for a flying wing configuration with variable longitudinal stability. *Aerospace Science and Technology*, 89:1–10, April 2019. http://www.sciencedirect.com/science/article/pii/S1270963819302548.

[25] Arne Voß and Thomas Klimmek. Maneuver Loads Calculation with Enhanced Aerodynamics for a UCAV Configuration. In *AIAA AVIATION Forum*, Washington, D.C., June 2016. American Institute of Aeronautics and Astronautics. http://arc.aiaa.org/doi/10.2514/6.2016-3838.

[26] Arne Voß and Thomas Klimmek. Design and sizing of a parametric structural model for a UCAV configuration for loads and aeroelastic analysis. *CEAS Aeronautical Journal*, 8(1):67–77, March 2017. https://link.springer.com/article/10.1007/s13272-016-0223-2.

[27] Arne Voß, Thomas Klimmek, and Kjell Bramsiepe. Design, Structural Optimization and Loads Assessment for a Flying Wing. Friedrichshafen, September 2018. Deutsche Gesellschaft für Luft- und Raumfahrt - Lilienthal-Oberth e.V. https://elib.dlr.de/121624/.

[28] Guido Voss, Sunpeth Cumnuantip, and Jens Neumann. A Steady Aeroelastic Analysis of an Unmanned Combat Aircraft Vehicle Conceptual Design. Honolulu, Hawaii, USA, June 2011. American Institute of Aeronautics and Astronautics. http://arc.aiaa.org/doi/10.2514/6.2011-3020.